



LAWRENCE
LIVERMORE
NATIONAL
LABORATORY

Optimization of strength and ductility in nanotwinned ultrafine grained Ag: twin density and grain orientations

R. T. Ott, J. Geng, M. F. Besser, M. J. Kramer, Y. M. Wang, E. S. Park, R. LeSar, A. H. King

June 7, 2016

Acta materialia

Disclaimer

This document was prepared as an account of work sponsored by an agency of the United States government. Neither the United States government nor Lawrence Livermore National Security, LLC, nor any of their employees makes any warranty, expressed or implied, or assumes any legal liability or responsibility for the accuracy, completeness, or usefulness of any information, apparatus, product, or process disclosed, or represents that its use would not infringe privately owned rights. Reference herein to any specific commercial product, process, or service by trade name, trademark, manufacturer, or otherwise does not necessarily constitute or imply its endorsement, recommendation, or favoring by the United States government or Lawrence Livermore National Security, LLC. The views and opinions of authors expressed herein do not necessarily state or reflect those of the United States government or Lawrence Livermore National Security, LLC, and shall not be used for advertising or product endorsement purposes.

Optimization of strength and ductility in nanotwinned ultra-fine grained Ag: twin density and grain orientations

R.T. Ott¹, J. Geng¹, M.F. Besser¹, M. J. Kramer^{1,2}, Y.M. Wang³, E. S. Park¹, R. LeSar^{1,2} and A. H. King¹

¹Division of Materials Sciences and Engineering, Ames Laboratory (DOE), Ames, IA 50011, USA

²Materials Science and Engineering Department, Iowa State University, Ames, IA 50011, USA

³Physical and Life Sciences Directorate, Lawrence Livermore National Laboratory, Livermore, CA 94550, USA

ABSTRACT

Nanotwinned ultrafine grained Ag thick films with different twin densities and orientations have been synthesized by magnetron sputtering with a wide-range of deposition rates. The twin boundary (TB) spacings and orientations as well as the grain size for the different deposition conditions have been characterized by both synchrotron X-ray scattering and transmission electron microscopy (TEM). Structural characterization combined with uniaxial tensile tests of the free-standing films reveals a large increase in the yield strength for films deposited at high deposition rates without any accompanying change in the TB spacing – a behavior that is in contrast with what has been reported in the literature. We find that films deposited at lower deposition rates exhibit more randomly oriented grains with a lower overall twin density (averaged over all the grains) than the more heavily twinned grains with strong $\langle 111 \rangle$ fiber texture in the films deposited at higher deposition rates. The TB spacing in the twinned grains, however, does not show any significant dependence on the deposition rate. The dependence of the strength and ductility on the twin density and orientations can be described by two different soft deformation modes: 1) untwinned grains and 2) nanotwinned grains that are not oriented with $\langle 111 \rangle$ along the growth direction. The untwinned grains provide relatively low resistance to slip, and thus decreased strength, while the nanotwinned grains that are not oriented with $\langle 111 \rangle$ along the growth direction are softer than nanotwinned grains that are oriented with $\langle 111 \rangle$ along the growth direction. We reveal that an ultrafine-grained (150-200 nm) structure consisting of a mixture of nanotwinned (~ 8 -12 nm spacing) and untwinned grains yields the best combination of high strength and uniform tensile ductility.

1. INTRODUCTION

Nanotwinned (nt) materials¹⁻⁵ have attracted considerable attention in recent years as an extension of work on nanocrystalline metals and alloys⁶⁻²³. While nanocrystalline materials exhibit significantly improved mechanical properties over materials with more conventionally-scaled microstructures, they

suffer from a number of challenges, including poor coarsening resistance and elevated electrical resistance²⁴⁻²⁶. Nanotwinned materials provide strength gains similar to those of their nanograined counterparts, but potentially with better coarsening resistance and improved electrical conductivity. The origins of the mechanical properties of nanotwinned materials, however, are not completely understood. Much has been learned about the effects of grain size on deformation. Strengthening of metals via the confinement of dislocations by grain boundaries can be described empirically by the Hall-Petch (H-P) relationship,

$$\sigma_y = \sigma_o + k_y d^{-1/2} \quad (1)$$

where σ_y is the yield strength, σ_o is related to the lattice friction, k_y is a constant and d is the grain size. This relationship has proven reliable over many orders of magnitude of the grain size, from the tens of microns down to nanocrystalline materials with grain sizes approaching 10-20 nm²⁷⁻³⁰. For smaller grain sizes, however, there is evidence from experiments and simulations that the H-P relationship breaks down, and there can be apparently “inverse H-P relationship” i.e., softening with decreasing grain size³¹⁻³⁶.

For face-centered cubic (fcc) metals that contain {111} coherent twin boundaries (CTB), the classic Hall-Petch equation in Eq.(1) has been modified to include the contribution of twins, which are now the smallest structural feature in the material. In this case, the revised H-P equation is:(9)

$$\sigma_y = \sigma_o k_y^d d^{-1/2} + k_y^t t^{-1/2} \quad (2)$$

where t is the average twin boundary spacing. For nt-Cu prepared by electrodeposition, Lu et. al reported that the tensile yield strength can be well-described by the H-P relationship in Eq. (2) down to a TB spacing of ~ 17 nm, at which point the films exhibit softening behavior¹⁴. Interestingly, nt-Cu films prepared by magnetron sputtering^{6,7,12,19,37} appear to show lower yield strengths than films prepared by electrodeposition for TB spacings down to ~ 15 nm, but no softening with decreasing TB spacing. A key difference between the two findings is that the films prepared by sputtering have strong <111> fiber textures and columnar grains, while the electrodeposited materials have mostly equiaxed nt-grains with more random orientations albeit still with a <111> fiber texture. The strength of the films with columnar grains has been described in the context of the confined layer slip (CLS) model, which was initially developed to describe plastic deformation in multi-layer films³⁸. Since the coherent TBs are predominantly parallel to the loading axis, according to the CLS model the yield strength should show a $1/t$ dependence^{19,39}.

Beyond size-dependent strengthening effects, texturing in polycrystalline materials is also known to strongly affect the strength of materials. For polycrystalline metals, the aggregate of grain orientations can be represented by the Taylor factor (M)⁴⁰, where,

$$\sigma = M \tau_{crss} \quad (3)$$

For fcc metals with random grain orientations, the average value for M is 3.1, but ranges from 2.5 to 3.67 for materials with 100% <100> texture and 100% <111> texture, respectively⁴¹. Given the strong

texturing often associated with films prepared by magnetron sputtering, the effects of the different grain orientations on the strengthening behavior need to be considered.

Although nanotwinned metals are known to have the ability to achieve both high strength and high ductility, the experimental demonstration of such a behavior has been limited to nt-Cu prepared by electrodeposition with random grain orientations¹⁴, where a minimum grain size of 500 nm is considered prerequisite in order to avoid the longstanding strength-ductility tradeoff enigma in nanostructured materials^{42,43}. An outstanding question remains whether both strength and ductility can be achieved when the grain size decreases below 500 nm as twin boundaries act as the main strengthening agents. There are existing challenges to investigate and subsequently optimize the strength-ductility of nt-metals in this grain size region (i.e., 100-500 nm). First, a large quantity of the data in the literature for ultrafine-grained materials has shown an early necking behavior and low uniform tensile elongation (<~2%) when the grain size is only a couple of hundred nanometers⁴². Second, to optimize the strength and ductility, a wide range of processing parameters is required in order to fabricate materials with different twin densities and grain sizes. Third, it is difficult to address the ductility issue through molecular dynamics (MD)⁴⁴, and thus experimental exploration of this behavior is essential. Lastly, there are a limited number of metals (e.g., copper, silver, and palladium), which form high-density growth twins during synthesis. Therefore, the material-of-choice for such study is very limited.

In this paper, the contributions of different strengthening mechanisms in nt-Ag films, e.g., grain size, twin density (averaged over all the grains) and orientation effects as well as their dependence on the processing conditions are examined. Specifically, we report on the strengthening associated with changing the TB density and orientation in free-standing nt-Ag films prepared by magnetron sputtering. Using a wide-range of deposition rates onto LN₂-cooled substrates, we are able to synthesize thick films (> 35 μ m) in which the average grain size can be tailored from 150 to 300 nm and the twin density varied for a constant TB spacing. Moreover, the relative orientations of the grains (and hence the twins) can be controlled, with the highest deposition rates yielding films with highly {111} textured columnar grains and the lowest deposition rates providing films with much more randomly oriented grains relative to the growth direction. From these films, we have determined the important interdependence between the deposition conditions, the twin density, twin orientations and the bulk mechanical behavior. For the first time, we achieve high strength and high ductility in a set of ultrafine-grained (150-200 nm) nt-Ag samples.

2. EXPERIMENTAL METHODS

Ag films were deposited onto <100> oriented Si wafers using magnetron sputtering. Three 50 mm diameter Ag targets were arranged in a confocal geometry to sputter onto the 152 mm diameter substrate, which was rotated at 15 revolutions per minute and cooled with liquid nitrogen, except where noted. The distance from the sputtering targets to the center of the substrate is 120 mm. For all of the sputtering runs, the base pressure was < 5 x 10⁻⁸ torr and the working pressure was 5 mtorr. The three sputtering guns were operated at 100, 175 and 300 W for the different deposition runs. For convenience, we will identify films by the respective gun powers at which they were sputtered (100,

175, 300 W). Due to the confocal geometry of the sputtering guns, a gradient of deposition rates develops across the radius of the substrate. These deposition rates were determined by measuring the film thickness (using micrometer) and dividing it by the deposition time. Figure 1(a) shows a schematic of the positions where samples were harvested for structural characterization and tensile testing. The sample positions are denoted by concentric circles (C1, C2, C3 and C4) of increasing radii from the center of the film that correspond to different deposition rates for a given sputtering power. Specifically, C1, C2, C3 and C4 correspond to radii of 10, 25, 40 and 55 mm, respectively, from the center of the substrate. For description purpose, we denote samples according to their deposition power and location as “x W C_y” (where x=100, 175, 300 and y=1, 2, 3, 4).

The as-deposited structures of the Ag films were examined using synchrotron X-ray scattering experiments performed at Sector 6-IDD of the Advanced Photon Source at Argonne National Laboratory. The experiments were performed in transmission mode with 100 keV (0.1234 Å) X-rays that were focused to a beam size of 70 x 100 μm². The X-ray exposures were collected using a GE amorphous Si detector (200 x 200 mm² pixel size) positioned at 1434.6 mm from the samples. The camera length was determined by fitting the pattern of SRM Si powder using Fit2D software⁴⁵. The scattering geometry coupled with the high-energy X-rays corresponds to scattering from planes that are essentially parallel to the film growth direction (in-plane scattering). Figure 1(b) shows a schematic of the sample geometry and the diffracting planes that are examined in the synchrotron experiments.

The average twin boundary spacing and grain sizes and orientations of the samples were measured using an FEI Tecnai G² F20-XT transmission electron microscopy (TEM) and electron backscatter diffraction (EBSD) imaging. The TEM was performed on cross-sectional samples of the films that were prepared by wedge-polishing followed by dual-ion beam milling. The inverse pole figures were determined by EBSD on the top (free-side) of the films using a JEOL JAMP-7830F field-emission-gun scanning-electron microscope (FEG–SEM) equipped with EDAX detector and TSL OIM data acquisition system.

The mechanical behavior of the films was examined by testing the free-standing films in uniaxial tension at a constant strain rate of $\dot{\epsilon} = 1 \times 10^{-4} \text{ s}^{-1}$. Dog-bone shaped samples (3 mm width x 6 mm gage length) were cut from the films using a die and a razorblade to avoid any surface artifacts associated with electro-discharge machining (EDM). Previous experiments have shown that EDM could cause grain coarsening in nanocrystalline materials⁴⁶. The samples were tested in a Zwicki Z2.5 tester equipped with a non-contact laser extensometer to measure the strain. A minimum of 3 samples were tested for each deposition rate to obtain representative statistics.

3. RESULTS AND DISCUSSION

3.1. Relationship of synthesis conditions to film structure.

The deposition rates of our films depend on the substrate location and the gun power. For any given gun power, films located in C1 (closest to the radial center) have the highest deposition rates, and those

in C4 (closest to the edge) have the lowest. For any substrate location, the highest gun power produces the highest deposition rate. Our processing conditions therefore produce a range of deposition rates from 5.4 nm/s (for the C1 location at 300 W gun power) to 1.5 nm/s (for the C4 location at 100 W). The rates for all substrate positions and gun powers are shown in Figure 2. Within the range of conditions that we have used, similar deposition rates can be obtained at different gun powers, as seen in Figure 2.

Figure 3 shows typical cross-sectional TEM images of the central thickness regions of three different nt-Ag films taken from substrate position C1, deposited at rates of 1.5, 3.2 and 5.4 nm/s (obtained using gun powers of 100, 175 and 300 W, respectively, as shown in Fig. 2). All of the films exhibit a high-density of nanotwins within sub-micron columnar grains. The {111} coherent boundaries of the nanotwins lie essentially perpendicular to the growth direction (i.e., parallel to substrate surface).

As discussed above, the TEM images shown in Figure 3 were taken from the center thickness of the deposited films, however, the high deposition rates and active cooling of the substrates produces a nucleation layer of fine, equiaxed, randomly oriented grains, $\sim 1\ \mu\text{m}$ thick, adjacent to the substrate. Beyond this nucleation layer, different structures can develop. Figure 4 shows cross-sectional TEM images for the C1 position of the 300 W film (5.4 nm/s) near the substrate interface and in the middle of the film thickness. The column width increases slightly from the bottom to the top of the film, increasing by a factor between 2 and 3 from bottom to top, while the average spacing between the nanotwins is essentially constant from the bottom to the top of the film. Therefore, since the TB spacing is not a function of distance from the film surfaces, and the grain size does not show a large dependence on this parameter, we have defined the overall structures of the respective films by the grain sizes and twin thicknesses observed in the middle of the films.

The variation of average grain size (measured as column width) and TB spacing with deposition rate are shown in Figure 5(a) and (b), respectively. In Figure 5(a), the grain size of the films shows a clear increase with increasing deposition rate before plateauing for rates above 4 nm/s, but the twin boundary spacing does not vary significantly as deposition rates change, though, as discussed below, they show variations between positions of the sample on the substrate. The most noticeable differences between films deposited at different rates are the size, shape and orientation of the columnar grains. For the high deposition rate film (5.4 nm/s) the grains are very columnar (i.e., elongated along the growth direction in which the length is larger than the width) in nature with a strong $\langle 111 \rangle$ texture, which means the vast majority of TBs are aligned normal to the growth direction and parallel to the plane of the film. In contrast, the lower deposition rate films (1.5 nm/s) exhibit a wider distribution of grain shapes and sizes that are more randomly oriented.

Although the TB spacing does not vary with deposition rate, we do observe variations according to substrate position (i.e., C1 vs. C4), as shown in Figure 5(b). Recall, the deposition rate is higher at the C1 position than the C4 position for a fixed gun power, but the deposition rate at the C4 position for a higher gun power will be higher than the deposition rate at the C1 position at a lower gun power (see Figure 2). To investigate if cooling rate differences across the wafer were the source of the different TB spacings, we sputtered one film at 300 W without any active LN_2 cooling. The average TB spacing at the C1 position for this film was $\sim 8\ \text{nm}$, similar to the measurement for the films deposited on Si wafers that

were actively cooled. The difference in TB spacing as function of wafer position therefore appears to be due to the geometry of the sputtering cathodes relative to the substrate. While sputtering is not a “line of sight” process; the flux is dependent on the alignment of the cathodes. In our configuration, the cathodes are in a confocal arrangement directed at the center of the substrate, and thus the C4 position on the substrate is outside the highest flux region. The difference in the incident angle of the deposited flux is the likely cause for the variation in the average twin boundary spacing.

To quantify the variations in the grain orientations with deposition rate, we performed synchrotron X-ray diffraction experiments at the Advanced Photon Source. X-ray exposures were collected for specimens taken from differing substrate radii for the 100, 175 and 300 W samples, which correspond to the deposition rates shown in Figure 2. Since the diffracted intensity is collected on an area detector, in-plane diffraction from 0 to 2π of azimuth can be collected, covering all angles between the tensile and transverse directions of the tensile test specimens. For the texture analysis, we are only reporting data for the planes normal to the loading axis, although all the in-plane orientations have been measured.

Nanotwinned fcc metal films deposited by magnetron sputtering are typically found to exhibit columnar grains with a strong $\langle 111 \rangle$ out-of-plane (or “fiber”) texture^{12,16,26,37,47,48}. For fcc metals, the two major peaks with a sufficiently strong structure factor to produce detectable diffraction peaks in this geometry are $\{220\}$ and $\{211\}$. Therefore, strong $\langle 111 \rangle$ out-of-plane texture should correspond to strong $\{110\}$ in-plane texture with a minimal amount of $\{111\}$ planes oriented in-plane. With this in mind, the ratio of the scattered intensity of the $\{220\}$ peak to the $\{111\}$ peak (normalized to random texture), as in

$$\Gamma = \frac{\left(\frac{I_{220}}{I_{111}}\right)_{film}}{\left(\frac{I_{220}}{I_{111}}\right)_{random}} = \frac{\left(\frac{I_{220}}{I_{111}}\right)_{film}}{0.25} \quad , \quad (6)$$

can be used as a simplified form of the Harris texture index⁴⁹, to quantify the intensity of the preferred $\langle 111 \rangle$ out-of-plane texture.

Figure 6 shows the measured in-plane texture parameter as a function of deposition rate for the films deposited at 100, 175 and 300 W. For the films deposited at 100 and 175W, the texture parameter increases slightly from C4 to C1, however, for the 300 W film, there is a very large jump in the texture parameter between positions C4 and C1. At this high overall deposition rate, the increase in deposition rate between C4 to C1 (from 4.4 to 5.4 nm/s) leads to a large increase in the $\langle 110 \rangle$ in-plane texturing, and thus, the $\langle 111 \rangle$ out-of-plane texturing.

3.2 Tensile behavior of nanotwinned films

The structure (e.g., grain size and morphology) of the Ag films exhibits a clear dependence on the deposition rate, allowing us to correlate the tensile behavior of the films with their structure. Dog-bone shaped samples for tensile testing were harvested from the free-standing films so that the growth direction was normal to the tensile axis [see Figure 1(b)]. The quasi-static ($\dot{\epsilon} = 1 \times 10^{-4} \text{ s}^{-1}$) stress-strain curves for the C1 circles (nearest the center) for the films deposited with deposition rates of 1.8, 3.2 and

5.4 nm/s (100, 175 and 300 W, respectively) are shown in Figure 7. The yield strength increases with increasing deposition rate, while the uniform tensile ductility declines. Representative fracture surfaces for the samples deposited at 1.8 and 5.4 nm/s are shown in Figure 8 (a) and (b), respectively. The lower deposition rate sample (1.8 nm/s) films shows a relatively smooth fracture surface that is characteristic of shear, while the higher deposition rate film (5.4 nm/s) exhibits a faceted fracture surface that is typically associated with more brittle intergranular fracture. The stress-strain curves show that the 100 W C1 (1.8 nm/s) sample does indeed show lower strength, but high tensile ductility compared to the strong, but relatively brittle, 300 W C1 (5.4 nm/s) sample. A summary of the tensile properties of the different films is provided in Table 1.

The relationships between the yield strength and the structure of these films yield several insights into the controlling mechanisms. Figure 4. TEM cross-section from (a) bottom of film at substrate interface and (b) top of film corresponding to free-side for C1 position of film deposited at 300 W (5.4 nm/s).

Figure 5 shows that the TB spacing is essentially independent of the deposition rate while the grain size increases with increasing deposition rate. The 100 W C1 sample deposited at a rate of 1.8 nm/s ($\sigma_y = 266$ MPa), corresponding to a TB spacing and grain size of 8 nm and 150 nm, respectively, while the average TB spacing and grain size for the 300 W C1 sample deposited at 5.4 nm/s ($\sigma_y = 510$ MPa) are 8 nm and 290 nm, respectively. Since the TB spacing does not show systematic dependence on the deposition rate, the increasing tensile strength for films deposited at higher rates cannot be described in the context of H-P or CLS strengthening. Furthermore, with the grain size and the strength increasing with increasing deposition rate, the mechanical behavior is contrary to H-P strengthening. Therefore, the strengthening exhibited by the films deposited at higher rates must be ascribed to other factors beyond size effects.

Our TEM observations showed that both the grain morphology (columnar or equiaxed) and grain orientations (and thus, TB orientations) are also dependent on the rate at which the films are deposited. Since the average TB spacing measurements are based on imaging conditions in which the TBs are visible, it is important to examine the overall TB densities of the different samples. As seen in Figure 3, the films deposited at low rates exhibit a mix of columnar grains with an average TB spacing that is approximately the same as that of the grains in the films deposited at high rates, along with smaller grains that do not show any obvious TBs. Closer examination of these smaller grains reveals that, unlike the heavily twinned columnar grains that exhibit $\{110\}$ in-plane orientations, the smaller grains exhibit more random in-plane orientations. Figure 9 shows a cross-sectional TEM image of a C1 sample for a film deposited at 100W (1.8 nm/s). The grain circled and marked “A” does not exhibit any obvious nanotwins, while the circled grain marked “B” is columnar in nature with numerous nanotwins. The accompanying diffraction patterns for the two grains show that grains A and B correspond to the electron beam parallel to the $[112]$ and $[011]$ directions, respectively. Since the $[011]$ direction is 30° relative to the $[112]$ direction, rotating the sample accordingly should make any $\{111\}$ CTBs in grain A visible. Figure 9 (c) and (d) show that rotations of 30° do not reveal the presence of any twins in grain A. Obviously TBs could be oriented at angles outside of the tilt conditions we examined, however, our experiments suggest that the TB densities are lower in the films deposited at lower rates. These results suggest that columnar grains oriented $\langle 111 \rangle$ parallel to the growth direction are most likely to form

nanotwins, while the smaller, more randomly oriented grains are less likely to form growth twins during deposition. Assuming this relationship is true for the Ag films, the strength of the films should be dependent on the density of <111> oriented columnar grains, which directly affects the twin density. The grains that do not contain growth twins should act as “soft grains” since they do not provide as great of resistance to dislocation motion, and thus, allow for easier slip.

The deposition rate dependence of the twin density is consistent with the thermodynamic model of growth twin formation in 330 SS/Cu multilayers that Zhang et al.²⁰ have proposed in which the critical nucleation radii for a perfect nuclei and a growth twin can be expressed according to:

$$r_{perfect}^* = \frac{\gamma}{\left(\frac{kT}{\Omega} \ln \left[\frac{J\sqrt{2\pi m kT}}{P_s} \right] \right)} \quad (4)$$

$$r_{twin}^* = \frac{\gamma}{\left(\frac{kT}{\Omega} \ln \left[\frac{J\sqrt{2\pi m kT}}{P_s} \right] - \frac{\gamma_t}{h} \right)} \quad , \quad (5)$$

in which γ is the surface energy, k is Boltzmann’s constant, T is the substrate temperature, Ω is the atomic volume, J is the deposition flux, m is the atomic mass of the deposited material, P_s is the vapor pressure of the condensed film, γ_t is the twin boundary energy and h is the nuclei height, assumed to be the (111) interplanar spacing. In this model, minimizing the difference between r_{twin}^* and $r_{perfect}^*$ promotes the formation of growth twins during deposition. For fixed stacking fault energy, the parameter that can be most readily adjusted is the deposition rate, J , which should decrease r_{twin}^* and, thus, promote nanotwin formation. This behavior is consistent with our experimental observations showing that higher deposition rates lead to higher twin densities by promoting more grains to form growth twins (instead of the decrease of twin spacings). It is important to note that this is simply a thermodynamic model that does not account for other factors such as growth stresses, but it does seem to be qualitatively consistent with our experimental observations.

3.3 Texture Effects on Deformation Behavior

As shown in Figure 6, the in-plane orientation of the grains in the Ag films is highly dependent on the deposition rate, especially at higher overall rates, as seen in samples deposited at 300W. Figure 10 (a) and (b) show the tensile yield stress and the maximum uniform tensile strain, respectively, as a function of the measured in-plane texture parameter, Γ . From this data, we can divide the strength-ductility behavior into two regions. Region I corresponds to relatively modest in-plane and out-of-plane texturing ($\Gamma < 5$) where the strength shows a distinct increase with small changes in the texture, while the uniform ductility exhibits a corresponding decrease. The enhanced strength at the expense of

uniform tensile ductility can be attributed to increasing TB density with higher deposition rates. The average TB spacing in the grains is not changing with increasing deposition rate (and thus, increasing texture parameter), but instead more grains are forming growth twins during deposition. For films deposited at higher rates, the TB density becomes saturated and the orientation of the grains (TBs) dominates the mechanical behavior. In region II ($I > 5$) the texture parameter exhibits a large increase, which corresponds to a maximum in the yield stress and a marked decrease in the tensile ductility.

The texture parameter is a measure of the predominance of grains oriented with $\{111\}$ planes normal to the growth direction and parallel to the loading axis. The twin boundaries in these films are predominantly coherent twin boundaries, parallel to the set of $\{111\}$ planes closest to the film plane, so the texture parameter is also a measure of the strength of alignment of the twins to the tensile axis. Figure 10 (a) thus indicates that the more the twin boundaries are parallel to the loading axis, the higher the tensile flow stress. To confirm this observation, EBSD patterns of the planar surfaces for samples deposited at 3.2 nm/s (175 W C1 position) and 5.4 nm/s (300 W C1 position) were taken, Figure 11(a) and (b), respectively. The EBSD pattern for the low deposition rate sample shows many more randomly oriented grains than the high deposition rate sample, which is strongly $\langle 111 \rangle$ textured. The higher degree of $\langle 111 \rangle$ texturing for high rate deposition is in good agreement with the synchrotron XRD measurements, which also shows that higher deposition rates correspond to much more $\langle 111 \rangle$ out-of-plane texturing in the films than do low deposition rates. It is important to note that just because a grain is not oriented $\langle 111 \rangle$ parallel to the growth direction does not mean it will not have growth twins present. In fact, for lower deposition grains, nanotwins can be seen in grains imaged in the planar orientation. Moreover, Bufford and coworkers found that a high density of nanotwins could be achieved in Ag films deposited epitaxially on $\langle 110 \rangle$ oriented Si wafers⁵⁰. Our findings do show, however, that the twin density appears to be highest when the grains have predominantly $\langle 111 \rangle$ orientation parallel to the growth direction.

The effect on the yield strength of twin orientation relative to the loading axis has been examined experimentally as well as by crystal plasticity models and MD simulations (JC Ye et al. APL 100, 261912, 2012; remove ref. 46?)^{19,39,51}. Although previous work does not take into account the grain orientation effects and thus is not directly comparable with the texture parameter measured in our work, the earlier results provide a point of comparison to our findings. You et al. have found that nt-Cu with a columnar structure exhibits H-P strengthening when the TBs are normal to the loading axis ($\sigma \sim t^{-1/2}$) but the strengthening is best described in the context of the confined layer slip model ($\sigma \sim t$) when the TBs are oriented parallel to the loading axis, as they are, predominantly, in our experiments. Furthermore, they used modeling to predict that materials with TBs oriented parallel to the loading axis are stronger than materials with TBs oriented 45° or normal to the loading axis^{19,39}. Defining the orientation of the TBs relative to the loading axis is relatively straightforward for modeling methods, but is much less easily defined and always subject to more or less broad distributions in experiments like ours. Using EBSD, You et al. found the $\langle 111 \rangle$ out-of-plane texture in their columnar nt-Cu films to be $\sim 6\times$ greater than that of a randomly textured sample, however, their images also show a distinct presence of twins oriented normal to the tensile axis¹⁹. Quantification of the inverse pole figure maps corresponding to Figure 11(a) and (b) show that films deposited at 1.5 nm/s (100 W C1) and 5.4 nm/s (300 W C1) exhibit out-of-plane

$\langle 111 \rangle$ texturing $\sim 6\times$ and $\sim 10\times$ greater than random, respectively. This is consistent with the in-plane texture parameters measured by synchrotron XRD, which show a significant difference between the two samples. Moreover, a particularly large increase in the strengthening occurs between 5-10x “random in-plane texture” (determined by XRD), but it is not possible to relate this measure of twin orientation to a particular twin inclination angle. Furthermore, it is not simple to characterize the twin densities for the samples, since the in situ XRD shows that a distinct fraction of grains for the different samples will be oriented such that the TBs cannot be readily seen in the cross-sectional view. Therefore, the presence (or absence) of TBs in every grain is difficult to be confirmed.

Dislocation interactions with different TB orientations have been examined in Cu by Ye et al.^{??} and You et al.^{??} via experiments and MD simulations, from which they found that there were hard and soft modes of deformation³⁹. For twin boundaries normal to the loading axis, the dislocations intersected and were trapped by the TBs, which was a hardest mode of deformation with increased strength. For TBs oriented parallel to the loading axis, threading dislocations were pinned between the adjacent TBs; this less hard mode of deformation was analogous to the CLS model. In contrast to above hard modes, the TBs inclined to the loading axis at an angle of 45° exhibited easy slip with much lower hardness, which they called a soft deformation mode. Our results for nt-Ag are consistent with the modeling results to the extent that the more textured (i.e., TBs parallel to loading axis) samples exhibit higher strength. Additional key differences for the films we studies include clearly more $\{111\}$ oriented grains and the soft deformation modes should be divided into 1) twinned and 2) untwinned grains that are not oriented $\langle 111 \rangle$ parallel to growth direction. As discussed above, for low deposition rates, some equiaxed, more randomly oriented grains do not have any obvious growth twins, which should allow for easy slip compared to the nanotwinned grains. For higher deposition rates, there are still some more-randomly oriented grains, but they are more likely to contain growth twins. These type of grains would be softer than the $\langle 111 \rangle$ oriented columnar twinned grains, but stronger than the untwinned grains.

3.4 Optimization of strength and ductility for nanotwinned Ag in ultrafine-grained region

Based upon our synthetic studies, it is difficult to separate out the grain orientation, twin density and orientation effects on the strengthen and ductility. As discussed above, however, the $\langle 111 \rangle$ texturing in Region I does not change significantly with increasing deposition rate, but the film strength (and ductility) does. High strengths in nanocrystalline and nanotwinned metals can be readily achieved by decreasing the grain size or twin boundary spacing, however maintaining ductility is much more difficult. Large work hardening is necessary to suppress flow softening and promote uniform tensile ductility in nanostructured materials. For nt-Cu films, the work hardening behavior is strongly dependent on both the TB spacing and the grain size^{52,53}. Lu et al., have reported that equiaxed Cu films with TB spacings below 100 nm exhibit minimal hardening when the average grain size approaches $\sim 1 \mu\text{m}$ ⁵³. Furthermore, they reported the lack of strain hardening, and thus, uniform tensile ductility is decreased for nt-Cu films with columnar grains^{52,53}.

For Region I of Figure 10 (a) and (b), the average TB spacing is < 15 nm for all of the samples and the average grain size ranges from 150-200 nm. This combination of very small TB spacing and grain sizes would be consistent with poor work hardening, i.e., low uniform tensile ductility, however, there is not a precipitous decrease in tensile ductility with increasing deposition rate for the samples shown in Region I of Figure 10(b). Figure 12 shows a comparison of the strength-ductility of our nt-Ag samples with the limited tensile data available in the literature for nanostructured Ag. The measured tensile yield stress as a function of uniform ductility for nt-Ag films (grain size 600 – 1000 nm²³ and 150-350 nm, present work) and UFG-Ag^{54,55} processed by equal channel angle pressing (ECAP) and asymmetric rolling (ASR) with grain sizes ranging from 200-300 nm are shown. First, when the texture parameter, Γ , is less than 5 [i.e., Region I in Figure 10(a) and (b)] the nt-Ag samples show a large uniform tensile ductility (>6.0%) with a strength increases of ~28% (from 256 MPa to 327 MPa) as the deposition rate increases from 1.5 to 3.2 nm/s. This sharp increase in strength without much sacrifice of uniform tensile ductility is likely attributed to the increased twin density due to the increased percentage of twinned grains. Second, as the texture parameter becomes larger than 5, we observe a sharp drop of the uniform tensile ductility to below ~3% despite the further increased strength. This clear loss of tensile ductility is coincident with the development of strong columnar ultrafine-grains. As illustrated in Figure 12, all the nt-Ag samples deposited at 2.6-3.2 nm/s rate exhibit a best combination of strength and ductility. This behavior is in contrast with that of most ultrafine-grained materials, which show a uniform tensile ductility of less than 2% when the grain size is between 150-200 nm⁵⁶. We note that high strength and high ductility has been achieved in nt-Cu with decreasing twin spacing but at much larger grain sizes (~500 nm). Our work here indicates that such high strength and high ductility can be achieved in much smaller grain sizes by controlling the percentage of twinned grains. Indeed such heterogeneous or hierarchical grain structured materials with growth or deformation twins have been a subject of current research⁵⁷.

To better understand this combined strength and ductility, we compared the strain hardening for samples from the three different regions Figure 12. The work hardening behavior for a sample can be quantified by plotting the work hardening rate ($\theta = d\sigma/d\varepsilon$) vs. the increase in the flow stress ($\sigma - \sigma_y$). This method is based on the Kocks-Mecking model^{58,59}, where

$$\theta = \theta_0 - K\sigma \quad [6]$$

θ_0 is a constant related to the dislocation storage and K is the slope of the linear part of the curve, which is a dynamic recovery parameter that is a measure of the thermally activated strain softening. Figure 13, shows the work hardening rate as function of the reduced true stress for the nt-Ag samples deposited at 1.8 nm/s (100 W C1), 3.2 nm/s (175 W C1) and 5.4 nm/s (300 W C1). Recall, that the samples deposited at 175 W exhibit the best combination of high strength and ductility in Figure 12. From the fitted K values of 68, 179 and 340 for the 100, 175 and 300 W samples, respectively, it is clear that the strain softening behavior for the nt-Ag samples is relatively high compared to coarse grained Ag. The high strain softening can be attributed to the columnar nature of the grains in which the TBs are

parallel to the tensile loading axis. In this geometry, plasticity occurs via threading dislocations between the TBs, which results in much lower work hardening than dislocation transmission across TBs. The measured texture parameter of the films Figure 6 shows that the columnar nature of the grains increases significantly for the films sputtered at 300W, which corresponds to the very high K value of 340. The samples sputtered at 100 and 175 W exhibit much smaller texture parameters, which are consistent with less columnar structures. This is reflected in the smaller K values and the larger measured uniform ductility. Interestingly, Sample (100 W C1) shows a lowest K value of 68, which is favorable for tensile ductility; but it also shows a low strength due to the low twin density (~65% of grains are twinned). This behavior suggests that a higher K value (i.e., a high recovery rate) is common for materials with both high strength and high ductility. The optimal microstructure we observe here contains ~95% twinned grains with relatively weak $\{111\}$ texture which promotes strain hardening at high stresses but also an enhanced recovery rate. How to strike a balance between strain hardening and dynamic recovery in these ultrafine-grained materials remains a subject of future computational studies.

4. CONCLUSIONS

In summary, we have synthesized nanotwinned ultrafine-grained Ag with different twin densities and orientations via magnetron sputtering. From the TEM and uniaxial tensile tests of the free-standing films, we find that there is a large increase in the yield strength of the films deposited at high deposition rate without any accompanying change in the TB spacing. Synchrotron XRD experiments performed on the films reveal that the texture, and thus, the TB orientations relative to the tensile axis are strongly dependent on the deposition rate as is the yield strength and tensile ductility. The films deposited at lower deposition rates exhibit more randomly oriented grains, which appear to have a lower twin density than the $\{111\}$ oriented columnar grains present in the films deposited at higher deposition rates. The dependence of the strength and ductility on the films can be broken down into two different types of soft deformation modes; 1) Untwinned and 2) Nanotwinned grains that are not oriented $\langle 111 \rangle$ along the growth direction. The former allows for easy slip compared to twinned grains, and thus decreased strength, while the latter is softer than nanotwinned grains that are oriented $\langle 111 \rangle$ along the growth the direction. Microstructures consisting of ultrafine-grains containing nanotwins with average twin boundary spacings of 8-12 nm dispersed in untwinned grains provide for the best combination of strength and tensile ductility.

Acknowledgement

The work at Ames Laboratory was supported by the U.S. Department of Energy, Office of Basic Energy Science, Division of Materials Sciences and Engineering under Contract No. DE-AC02-07CH11358. The work at Lawrence Livermore National Laboratory (Y.M. Wang) was supported by the U.S. Department of Energy under Contract DE-AC52-07NA27344. The Advanced Photon Source at Argonne National Laboratory was supported by the U.S. Department of Energy under Contract DE-AC02-06CH11357.

Table 1:

Sample	Deposition Rate (nm/s)	TB Spacing (nm)	Grain Size (nm)	Estimated percentage of twinned grains	Yield Stress (0.2 %)	Max. Uniform Strain (%)
100 W C4	1.5	12 ± 6	150		266 ± 18	8.0 ± 1.4
100 W C3	1.6				256 ± 7	9.0 ± 1.4
100 W C2	1.7				258 ± 14	8.5 ± 1.4
100 W C1	1.8	8 ± 4	140	~65%	266 ± 15	8.5 ± 1.8
175 W C4	2.6	11 ± 6	200		325 ± 21	6.7 ± 0.7
175 W C3	2.8				322 ± 27	6.7 ± 0.6
175 W C2	3.0				327 ± 22	6.0 ± 0.6
175 W C1	3.2	7 ± 4	171	~90%	327 ± 39	6.7 ± 1.6
300 W C4	4.4	12 ± 9	300		386 ± 31	3.1 ± 1.0
300 W C3	4.8				455 ± 60	2.4 ± 0.8
300 W C2	5.2				517 ± 7	2.7 ± 0.9
300 W C1	5.4	8 ± 4	290	~100%	510 ± 12	2.3 ± 0.6
300 W C1	– No Cool-	8 ± 5	272			

Figs:

Figure 1. (a) Schematic of circles (C1, C2, C3 and C4) corresponding to different deposition rates along the film. Samples for structural characterization and mechanical testing were harvested from the different circle positions. (b) Image of dog-bone shaped sample used in tensile tests and the in situ synchrotron experiments. The orientation of the twin boundaries to the tensile loading axis is shown.

Figure 2. Measured deposition rate as function of radial position along substrate for different for films sputtered at 100, 175 and 300 W, respectively.

Figure 3. TEM cross-sectional images for samples taken from C1 position for (a) 100 W (1.8 nm/s) , (b) 175 W (3.2 nm/s) and (c) 300 W (5.4 nm/s) films.

Figure 4. TEM cross-section from (a)bottom of film at substrate interface and (b) top of film corresponding to free-side for C1 position of film deposited at 300 W (5.4 nm/s).

Figure 5. Average (a) grain size and (b) twin boundary spacing as a function of deposition rate for films deposited at 100, 175 and 300 W. The grain size is the average width of the columnar grains measured from cross-sectional TEM.

Figure 6. In-plane texture parameter (Γ) determined by synchrotron XRD as a function of deposition rate for the Ag films. Here, higher texture parameter values (i.e., higher $\langle 110 \rangle$ in plane texture) correspond to large $\langle 111 \rangle$ out-of-plane texture.

Figure 7. (a)Uniaxial tensile stress-strain curves ($\dot{\epsilon} = 1 \times 10^{-4} \text{ s}^{-1}$) for C1 positions of films deposited at different rates. The true stress (σ_T) was calculated from the engineering stress, and therefore, is only valid prior to necking.

Figure 8. Fracture surfaces from C1 position of films deposited at (a) 1.8 nm/s and (b) 5.4 nm/s, respectively. The low deposition rate film, which corresponds to lower strength and large plastic strain in Fig. 7, exhibits a shear-like fracture

surface. The high deposition rate film, which corresponds to high strength and low plasticity in Fig. 7, exhibits more faceted fracture surface.

Figure 9. (a) Cross-sectional TEM image of film deposited at 1.8 nm/s (C1 100 W). A grain with no obvious twin boundaries is labeled A and a grain with a high density of twin boundaries is labeled B. For the two denoted grains the electron beam is parallel to the [112] and [011] directions, respectively. Figure 9 (c) and (d) show that rotations of 30° do not reveal the presence of any twins in grain A. No obvious TBs can be seen in grain A after rotation the sample 30° relative to the beam, (b) and (c).

Figure 10. (a)Yield strength and (b) uniform tensile ductility determined by quasi-static tensile tests as a function of the in-plane texture (Γ) measured by XRD.

Figure 11. Basckscatter electron diffraction orientation image maps for film corresponding to films deposited at (a) 1.8 nm/s (C1 100 W) and (b) 5.4 nm/s (C1 300 W).

Figure 12. Measured 0.2% yield stress as a function of uniform tensile ductility for nt-Ag films prepared by magnetron sputtering: blue squares, our work and red circles²³; UFG Ag prepared by equal channel angular pressing (ECAP): green triangle⁵⁵ and magenta diamond⁵⁴ and UFG Ag prepared by Asymmetric Rolling (ASR): blue star⁵⁵. All samples were tested at $\dot{\epsilon} \sim 10^{-4} \text{ s}^{-1}$ except the data from ²³ which was performed at $\dot{\epsilon} \sim 10^{-3} \text{ s}^{-1}$.

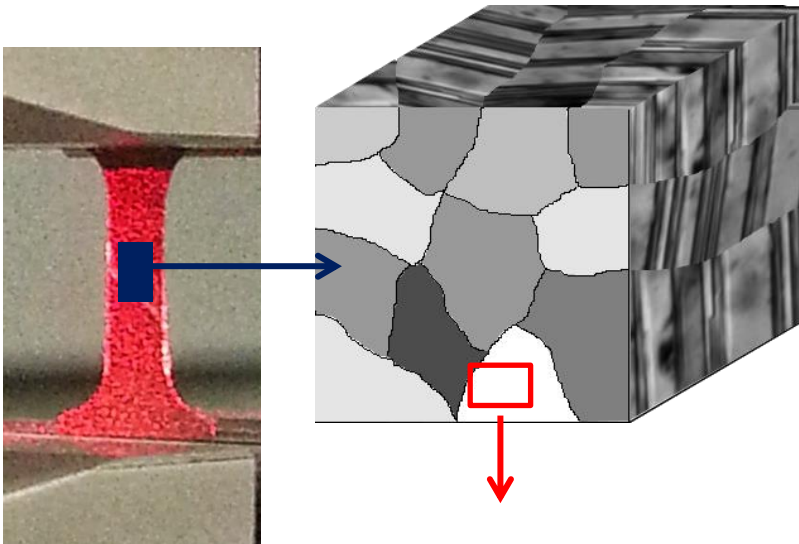
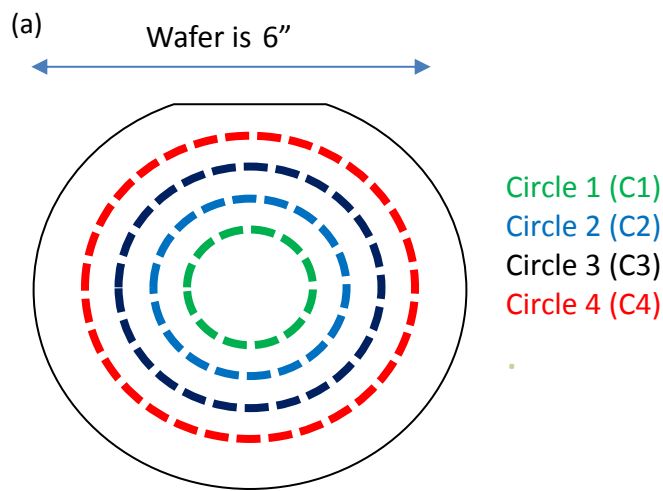
Figure 13. Work hardening rate ($\theta = d\sigma/d\epsilon$) as a function of reduced true stress for nt-Ag films deposited at 1.8 (C1 100 W), 3.2 (C1 175 W) and 5.4 nm/s (C1 300 W). The slope of the fitted linear regions of the samples is equal to $-K$ in Eqn 6.

- (1) Bufford, D.; Liu, Y.; Wang, J.; Wang, H.; Zhang, X. *Nature Communications* **2014**, 5.
- (2) Jang, D.; Li, X.; Gao, H.; Greer, J. R. *Nature Nanotechnology* **2012**, 7, 594.
- (3) Wang, Y. M.; Sansoz, F.; LaGrange, T.; Ott, R. T.; Marian, J.; Barbee, T. W., Jr.; Hamza, A. V. *Nature Materials* **2013**, 12, 697.
- (4) Beyerlein, I. J.; Zhang, X.; Misra, A. *Annula Review of Materials Research* **2014**, 44, 329.
- (5) Colla, M. S.; Amin-Ahmadi, B.; Idrissi, H.; Malet, L.; Godet, S.; Raskin, J. P.; Schryvers, D.; Pardoen, T. *Nature Communications* **2015**, 6, 5922.
- (6) Anderoglu, O.; Misra, A.; Wang, H.; Ronning, F.; Hundley, M. F.; Zhang, X. *Applied Physics Letters* **2008**, 93.
- (7) Anderoglu, O.; Misra, A.; Wang, H.; Zhang, X. *Journal of Applied Physics* **2008**, 103.
- (8) Cao, A. J.; Wei, Y. G. *Journal of Applied Physics* **2007**, 102.
- (9) Hodge, A. M.; Furnish, T. A.; Navid, A. A.; Barbee, T. W. *Scripta Materialia* **2011**, 65, 1006.
- (10) Hodge, A. M.; Furnish, T. A.; Shute, C. J.; Liao, Y.; Huang, X.; Hong, C. S.; Zhu, Y. T.; Barbee, T. W.; Weertman, J. R. *Scripta Materialia* **2012**, 66, 872.
- (11) Hodge, A. M.; Wang, Y. M.; Barbee, T. W. *Materials Science and Engineering a-Structural Materials Properties Microstructure and Processing* **2006**, 429, 272.
- (12) Hodge, A. M.; Wang, Y. M.; Barbee, T. W. *Scripta Materialia* **2008**, 59, 163.
- (13) Li, X.; Wei, Y.; Lu, L.; Lu, K.; Gao, H. *Nature* **2010**, 464, 877.
- (14) Lu, L.; Chen, X.; Huang, X.; Lu, K. *Science* **2009**, 323, 607.
- (15) Lu, L.; Dao, M.; Zhu, T.; Li, J. *Scripta Materialia* **2009**, 60, 1062.
- (16) Pan, Q. S.; Lu, Q. H.; Lu, L. *Acta Materialia* **2013**, 61, 1383.
- (17) Shan, Z. W.; Lu, L.; Minor, A. M.; Stach, E. A.; Mao, S. X. *Jom* **2008**, 60, 71.
- (18) Xu, D.; Kwan, W. L.; Chen, K.; Zhang, X.; Ozolins, V.; Tu, K. N. *Applied Physics Letters* **2007**, 91.
- (19) You, Z. S.; Lu, L.; Lu, K. *Acta Materialia* **2011**, 59, 6927.

- (20) Zhang, X.; Misra, A.; Wang, H.; Shen, T. D.; Nastasi, M.; Mitchell, T. E.; Hirth, J. P.; Hoagland, R. G.; Embury, J. D. *Acta Materialia* **2004**, *52*, 995.
- (21) Bufford, D.; Bi, Z.; Jia, Q. X.; Wang, H.; Zhang, X. *Applied Physics Letters* **2012**, *101*.
- (22) Bufford, D.; Wang, H.; Zhang, X. *Acta Materialia* **2011**, *59*, 93.
- (23) Furnish, T. A.; Hodge, A. M. *APL Materials* **2014**, *2*.
- (24) Brandstetter, S.; Zhang, K.; Escudro, A.; Weertman, J. R.; Van Swygenhoven, H. *Scripta Materialia* **2008**, *58*, 61.
- (25) Detor, A. J.; Schuh, C. A. *Journal of Materials Research* **2007**, *22*, 3233.
- (26) Anderoglu, O.; Misra, A.; Ronning, F.; Wang, H.; Zhang, X. *Journal of Applied Physics* **2009**, *106*.
- (27) Erb, U. *Nanostructured Materials* **1995**, *6*, 533.
- (28) Hughes, G. D.; Smith, S. D.; Pande, C. S.; Johnson, H. R.; Armstrong, R. W. *Scripta Metallurgica* **1986**, *20*, 93.
- (29) Detor, A. J.; Schuh, C. A. *Acta Materialia* **2007**, *55*, 371.
- (30) Schuh, C. A.; Nieh, T. G.; Iwasaki, H. *Acta Materialia* **2003**, *51*, 431.
- (31) Schiotz, J.; Jacobsen, K. W. *Science* **2003**, *301*, 1357.
- (32) Schuh, C. A.; Nieh, T. G.; Yamasaki, T. *Scr. Mater.* **2002**, *46*, 735.
- (33) Trelewicz, J. R.; Schuh, C. A. *Acta Materialia* **2007**, *55*, 5948.
- (34) Wolf, D.; Yamakov, V.; Phillpot, S. R.; Mukherjee, A.; Gleiter, H. *Acta Materialia* **2005**, *53*, 1.
- (35) Wolf, D.; Yamakov, V.; Phillpot, S. R.; Mukherjee, A. K. *Zeitschrift Fur Metallkunde* **2003**, *94*, 1091.
- (36) Yamakov, V.; Wolf, D.; Phillpot, S. R.; Mukherjee, A. K.; Gleiter, H. *Philosophical Magazine Letters* **2003**, *83*, 385.
- (37) Zhang, X.; Wang, H.; Chen, X. H.; Lu, L.; Lu, K.; Hoagland, R. G.; Misra, A. *Applied Physics Letters* **2006**, *88*.
- (38) Nix, W. *MTA* **1989**, *20*, 2217.
- (39) You, Z. S.; Li, X. Y.; Gui, L. J.; Lu, Q. H.; Zhu, T.; Gao, H. J.; Lu, L. *Acta Materialia* **2013**, *61*, 217.
- (40) Taylor, G. I. *J. Inst. Metals* **1938**, *62*, 307.
- (41) Meyers, M. A.; Chawala, K. K. *Mechanical Behavior of Materials*; Prentice-Hall, Inc.: New Jersey, 1999.
- (42) Wang, Y.; Chen, M.; Zhou, F.; Ma, E. *Nature (London, United Kingdom)* **2002**, *419*, 912.
- (43) Dao, M.; Lu, L.; Asaro, R. J.; De Hosson, J. T. M.; Ma, E. *Acta Materialia* **2007**, *55*, 4041.
- (44) Kulkarni, Y.; Asaro, R. J. *Acta Materialia* **2009**, *57*, 4835.
- (45) Hammersley, A. P.; Svensson, S. O.; Hanfland, M.; Fitch, A. N.; Hausermann, D. *High Pressure Res.* **1996**, *14*, 235.
- (46) Wang, Y. M.; Ott, R. T.; van Buuren, T.; Willey, T. M.; Biener, M. M.; Hamza, A. V. *Physical Review B* **2012**, *85*.
- (47) Zhang, X.; Anderoglu, O.; Hoagland, R. G.; Misra, A. *Jom* **2008**, *60*, 75.
- (48) Zhang, X.; Misra, A. *Scripta Materialia* **2012**, *66*, 860.
- (49) Harris, G. B. *Philosophical Magazine* **1952**, *43*, 113.
- (50) Bufford, D.; Wang, H. Y.; Zhang, X. H. *Journal of Materials Research* **2013**, *28*, 1729.
- (51) Zhang, S.; Zhou, J. Q.; Wang, L.; Wang, Y. *Materials & Design* **2013**, *45*, 292.
- (52) Chen, X. H.; Lu, L.; Lu, K. *Scripta Materialia* **2011**, *64*, 311.
- (53) Lu, L.; You, Z. S.; Lu, K. *Scripta Materialia* **2012**, *66*, 837.
- (54) Angella, G.; Bassani, P.; Farè, S.; Lecis, N.; Ripamonti, D.; Spagnoli, F.; Tuissi, A.; Vedani, M. In *Materials Science Forum* 2012; Vol. 706-709, p 1847.

- (55) Angella, G.; Esfandiari Jahromi, B.; Vedani, M. *Materials Science and Engineering: A* **2013**, 559, 742.
- (56) Wang, Y. M.; Ma, E.; Chen, M. W. *Applied Physics Letters* **2002**, 80, 2395.
- (57) Wei, Y.; Li, Y.; Zhu, L.; Liu, Y.; Lei, X.; Wang, G.; Wu, Y.; Mi, Z.; Liu, J.; Wang, H.; Gao, H. *Nat Commun* **2014**, 5.
- (58) Mecking, H.; Kocks, U. F. *Acta Metallurgica* **1981**, 29, 1865.
- (59) Kocks, U. F.; Mecking, H. *Progress in Materials Science* **2003**, 48, 171.

Fig 1.



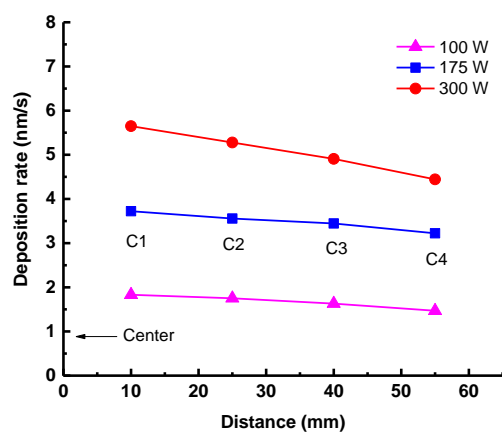
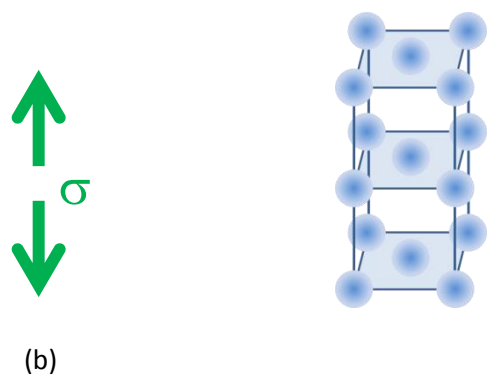
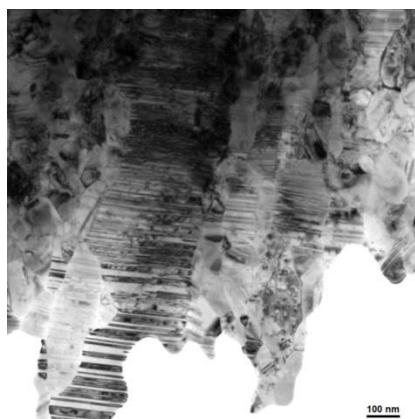
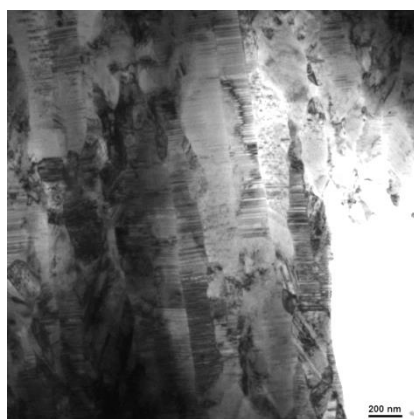


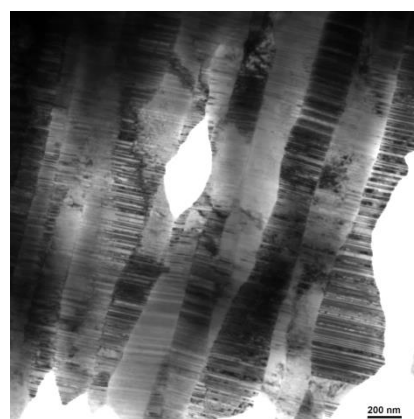
Fig. 2



(a)

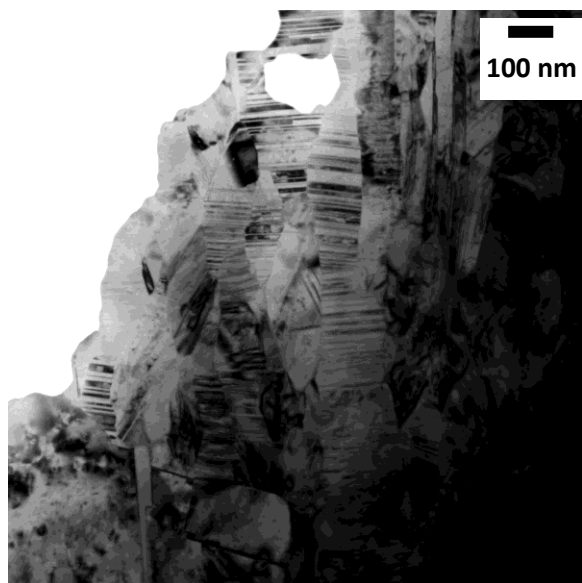


(b)

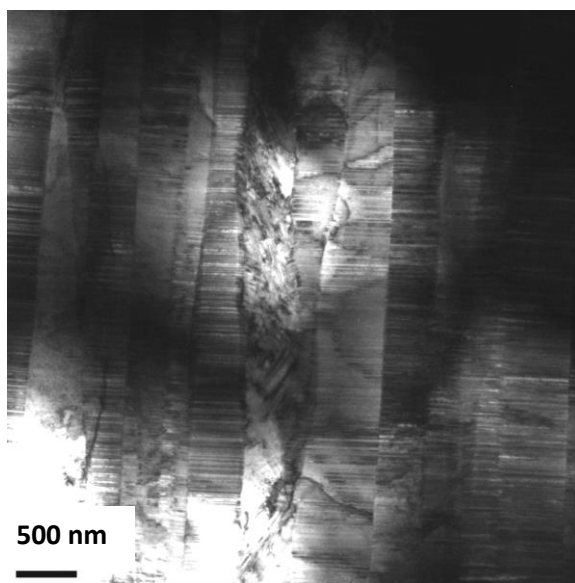


(c)

Fig. 3

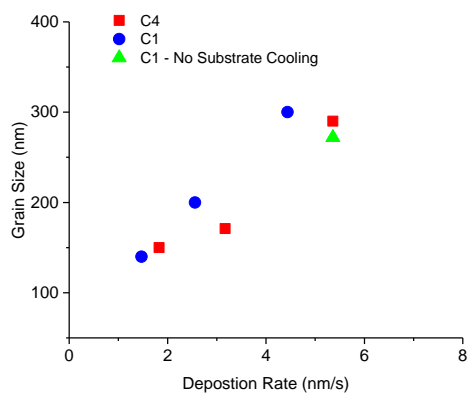


(a)

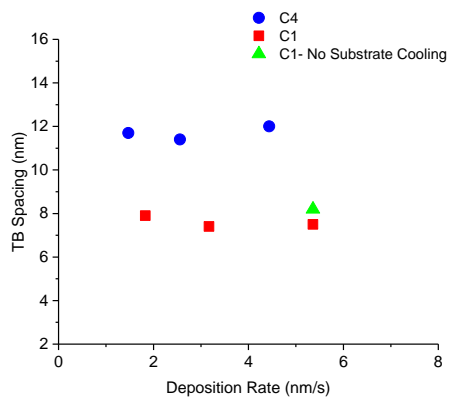


(b)

Fig. 4



(a)



(b)

Fig. 5

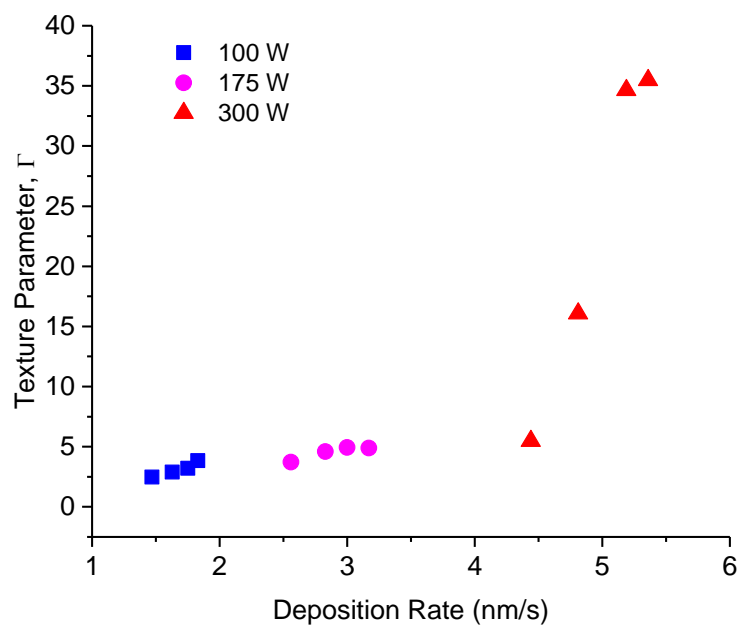


Fig. 6

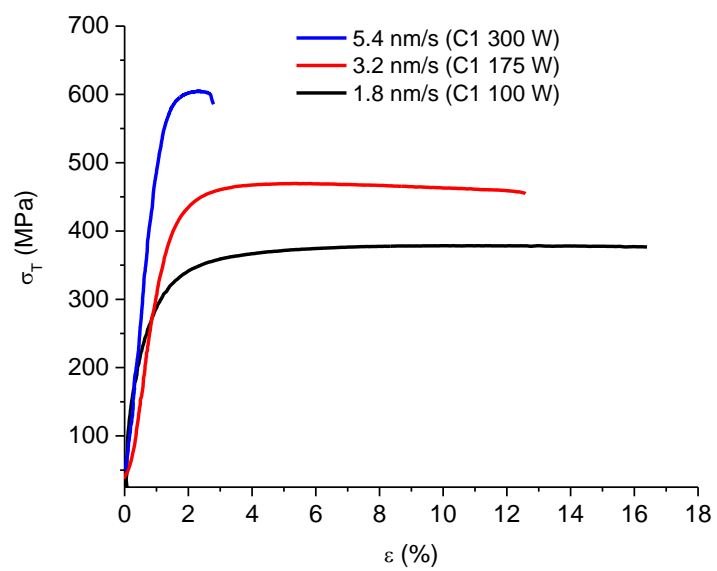
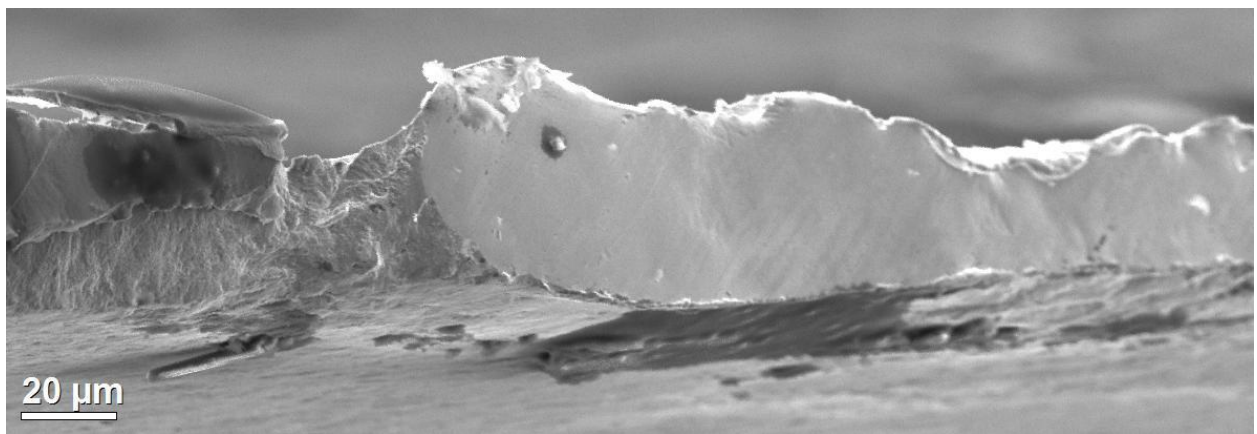
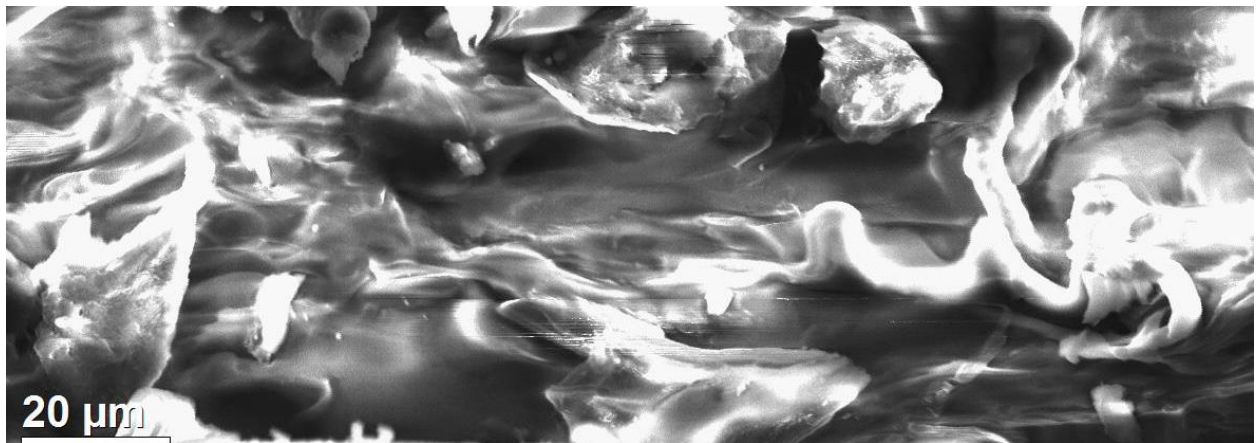


Fig. 7

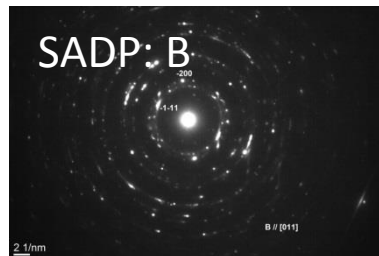
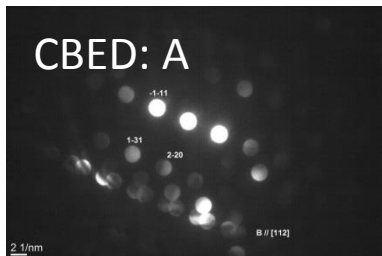
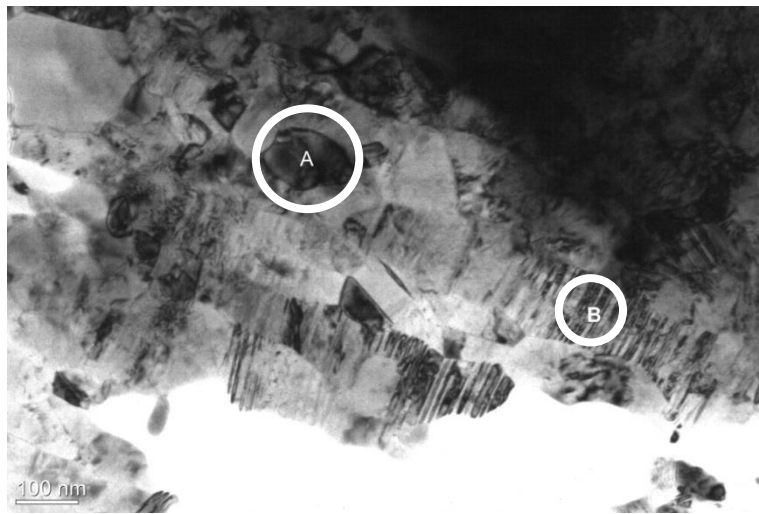


(a)



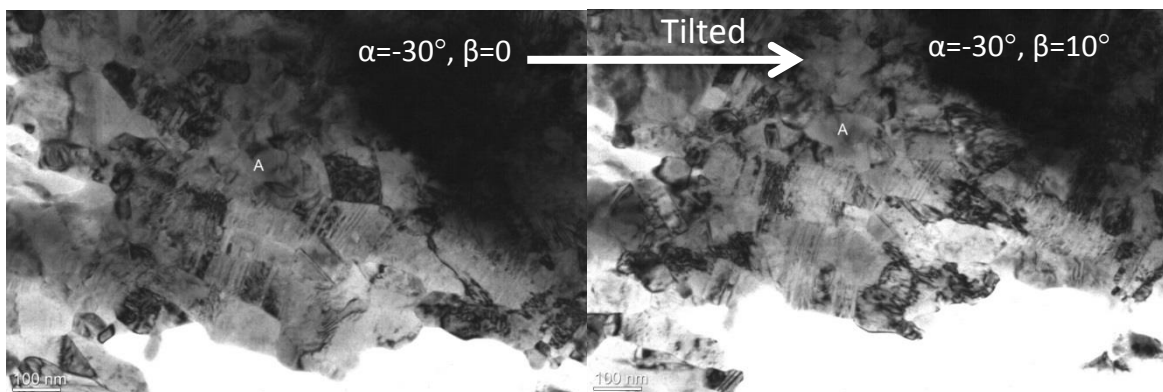
(b)

Fig. 8



(a)

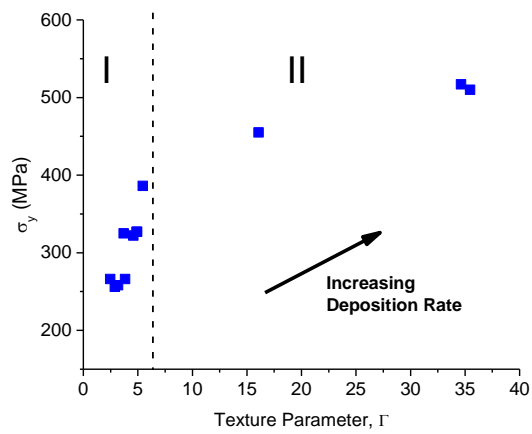
(a)



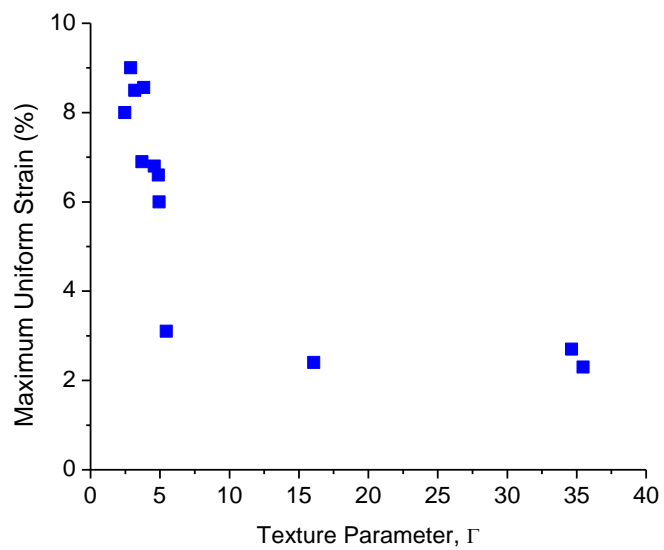
(b)

(c)

Fig. 9

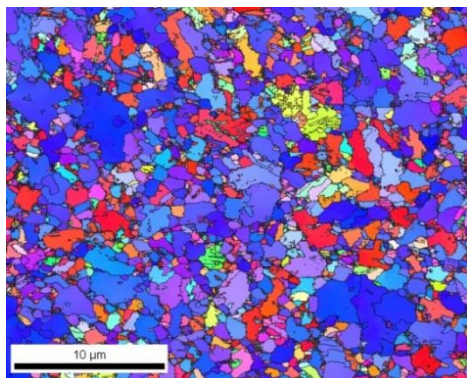


(a)

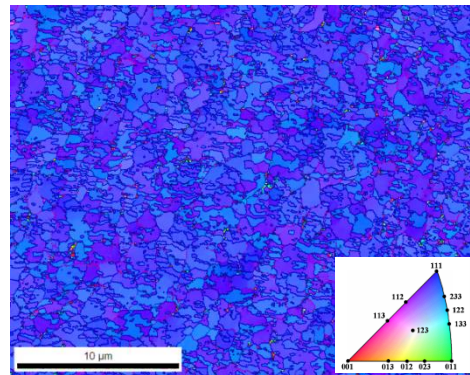


(b)

Fig. 10



(a)



(b)

Fig. 11 .